Lawrence Berkeley National Laboratory

Title

Nonperturbative study of bulk photovoltaic effect enhanced by an optically induced phase transition

Permalink

Journal

ISSN

Authors

Rajpurohit, Sangeeta
Pemmaraju, C Das
Ogitsu, Tadashi
et al.

Publication Date

DOI

Copyright Information

Peer reviewed

A non-perturbative study of bulk photovoltaic effect enhanced by an optically induced phase transition

Sangeeta Rajpurohit,[1, *] C. Das Pemmaraju,[2] Tadashi Ogitsu,[3] and Liang Z Tan[1]

[1]*Molecular Foundry, Lawrence Berkeley National Laboratory, USA*
[2]*Stanford Institute for Materials & Energy Sciences, SLAC National Accelerator Laboratory, USA*
[3]*Lawrence Livermore National Laboratory, Livermore, USA*

(Dated: May 25, 2021)

Solid systems with strong correlations and interactions under light illumination have the potential for exhibiting interesting bulk photovoltaic behavior in the non-perturbative regime, which has remained largely unexplored in the past theoretical studies. We investigate the bulk photovoltaic response of a perovskite manganite with strongly coupled electron-spin-lattice dynamics, using real-time simulations performed with a tight-binding model. The transient changes in the band structure and the photoinduced phase transitions, emerging from spin and phonon dynamics, result in a nonlinear current versus intensity behavior beyond the perturbative limit. The current rises sharply across a photoinduced magnetic phase transition, which later saturates at higher light intensities due to excited phonon and spin modes. The predicted peak photoresponsivity is orders of magnitude higher than other known ferroelectric oxides such as BiFeO$_3$. We disentangle phonon-and spin-assisted components to the ballistic photocurrent, showing that they are comparable in magnitude. Our results illustrate a promising alternative way for controlling and optimizing the bulk photovoltaic response through the photoinduced phase transitions in strongly-correlated systems.

The bulk photovoltaic effect (BPVE) is the generation of photocurrent in the bulk of a material, in the absence of any extrinsic carrier separation mechanism such as heterojunctions, and arising purely from its intrinsic non-centrosymmetry. As BPVE is not subject to the usual constraints of conventional p-n junction photovoltaics, such as the Shockley-Queisser limit, it has promising applications in next-generation light-harvesting and sensing. Shift currents and phonon-induced ballistic currents are two main mechanisms that have been put forward to explain BPVE in recent years, with relative magnitudes that are strongly dependent on crystal structure and materials system [1]. Shift currents [2–6] arise from the asymmetry of the nonlinear interactions of carriers with the light field. The ballistic currents are caused by the asymmetry of the momentum distributions of charge carriers [7–9] in non-centrosymmetric materials.

Complex materials with tuneable interactions and correlations are a promising class of systems to control and optimize the BPVE. Previous theoretical studies of BPVE are mostly based on perturbative methods [4, 5, 9–11]. These theories fail to describe photovoltaic behavior of such materials in non-perturbative regime where the charge dynamics is strongly coupled to phonon and spin dynamics. In this paper, we take a non-perturbative approach for studying the BPVE, to investigate its behavior in a strongly-correlated system as light intensity is increased continuously from the perturbative regime to current saturation. While perturbative calculations of the shift and ballistic currents are mostly performed by keeping the band structure and scattering matrix of carriers fixed, this rigid-band approximation can potentially break down as the light intensity is increased. For

instance, electron-phonon interactions can result in deviations from lowest-order behavior [11, 12]. This is of particular relevance for strongly-correlated systems with charge carriers dressed in the form of excitons, polarons, and magnons [13–19]. To include the dynamical effects [20, 21] arising due to the changes in the local symmetries and the band structure, we simulate the real-time evolution of the electron, spin and lattice degrees of freedom.

We study the BPVE of a strongly-correlated perovskite manganite A$_{1-x}$A$'_x$MnO$_3$ (A=La, Pr and A'=Ca) at doping $x = 2/3$ [22–24]. In its ground state, this system is in a bi-stripe (BS) phase, and is an improper ferroelectric with a weak polarization, exhibiting charge order (CO) and orbital order (OO). We report that its photocurrent has a strongly nonlinear dependence on intensity, stemming from a photoinduced magnetic phase transition that occurs during the optical excitation itself. Couplings to charge, spin, and phonon degrees of freedom are each necessary for this photoinduced phase transition. These results show that the consideration of phonon and spin dynamics are necessary for designing materials with tunable BPVE properties.

In A$_{1-x}$A'$_x$MnO$_3$ (A=rare-earth metal and A'=alkaline-earth metal) the octahedral crystal field splits the Mn 3d-shell into three nonbonding t_{2g}-orbitals and two antibonding e$_g$-orbitals. We treat the delocalized e$_g$-orbitals using a tight-binding model, and the localized t_{2g}-electrons as classical spins $\vec{S}_R$ with length $|S| = 3/2$ for each Mn-ion R.

The potential energy of the system is expressed as

$$E_{pot}\left(|\psi_n\rangle, \vec{S}_R, Q_{i,R}\right) = E_e(|\psi_n\rangle) + E_S(\vec{S}_R) + E_{ph}(Q_{i,R})$$

$$+ E_{e-ph}(|\psi_n\rangle, Q_{i,R}) + E_{e-S}(|\psi_n\rangle, \vec{S}_R) \quad (1)$$

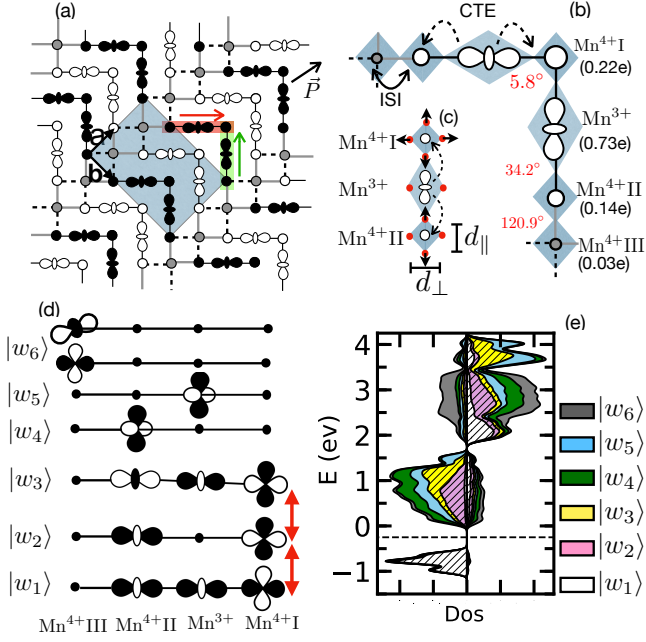FIG. 1. a): CO, OO, and SO of BS phase within the ab-plane. The circles and $d_{3x^2-r^2}/d_{3x^2-r^2}$-like orbitals are Mn^{4+} and Mn^{3+} sites, respectively. Black, white and gray indicates sites with different t_{2g}-spin orientation. The red (green) arrow indicates the local polarization direction of the horizontal (vertical) trimer and the black arrow indicate the net polarization $\vec{P}$ in the ab-plane. b): enlarged view of a pair of orthogonal adjacent trimer segments Mn^{4+} I – Mn^{3+} – Mn^{4+} II with additional Mn^{4+} III site indicating local e_g-electron densities (values in brackets) and intersite spin-angles (values in red). The solid and dashed arrows indicate charge transfer excitation (CTE) and photoinduced inter-site interaction (ISI). c): displacement (shown by arrows) of oxygen ions (red circles) following the photo-excitation. d): nature of Wannier states $|w_i\rangle$ where $i \in \{1, 2, ...6\}$. The red-arrows show inter-trimer dipole-allowed transitions. e): density of states for e_g d-states of Mn atoms projected on $|w_i\rangle$-states. The right- and left-side shows majority- and minority-spin states, respectively and the dashed line is the Fermi level.

in terms of one-particle states $|\psi_n\rangle = \sum\limits_{\sigma,\alpha,i} |\chi_{\sigma,\alpha,i}\rangle \psi_{\sigma,\alpha,i,n}$ of e_g-electrons, t_{2g}-spin $\vec{S}_R$ and oxygen octahedral $Q_{i,R}$ phonon modes. The basis set $|\chi_{\sigma,\alpha,i}\rangle$'s for the one-particle states consists of local spin-orbitals with spin $\sigma \in \{\uparrow,\downarrow\}$ and the orbital character $\alpha \in d_{x^2-y^2}, d_{3z^2-r^2}$.

The e_g-electrons delocalize between Mn sites via intermediate oxygen bridges. The electrons experience an on-site Coulomb interaction, a Hund's coupling from t_{2g}-spin $\vec{S}_R$ and an electron-phonon (el-ph) coupling with three local phonon modes per Mn-site. The phonon modes are the octahedral breathing $Q_{1,R}$, and the two Jahn-Teller (JT) active modes $Q_{2,R}$ and $Q_{3,R}$. These modes are highly cooperative due to the oxygen atoms shared between adjacent MnO_6 octahedra. The t_{2g}-spins $\vec{S}_R$ encounters an antiferromagnetic intersite coupling. For the

complete details of the model and its parameters, we refer to [25–27].

We predict that the BS phase has a stable non-collinear spin order (SO) in its ground state, illustrated in top-left Figure 1, which is lower in energy than previously reported collinear SOs [28]. The ordering within ab-planes can be seen as an arrangement of horizontal and vertical 'trimers', which are three almost ferromagnetically aligned Mn-sites, with average spin angles of $5.8°$ and $34.2°$, in a row Mn^{4+} I – Mn^{3+} – Mn^{4+} II. There are additional Mn^{4+} III sites that are not part of trimers. In the $\vec{c}$ direction, the SO is antiferromagnetic. The BS ground state is noncentrosymmetric with a calculated net polarization of $15\,nC/cm^2$ in the $\vec{a}$ direction (more information in SI).

The electronic structure of the BS phase can be explained in terms of Wannier states $|w_i\rangle$ ($i \in \{1, 2...6\}$) (details in SI), spanning the Hilbert space of the trimer segments and Mn^{4+} sites, see Figure 1d (more details in SI). The band-gap between the occupied $|w_1\rangle$-states and the other unoccupied $|w_i\rangle$-states arises predominantly from the JT splitting at Mn^{3+} sites and is highly sensitive to the octahedral modes. The doubly degenerate $|w_6\rangle$ are two e_g-orbitals of Mn^{4+} III sites. The density of states projected on the $|w_i\rangle$-states, shown in Figure 1e, clearly indicates the valence band consists of the bonding state of trimers, i.e., $|w_1\rangle$-states, with maximum weight on the central Mn^{3+} sites. Above the Fermi level are the nonbonding $|w_2\rangle$-states localized on the Mn^{4+} I and II terminal sites. Under optical excitation, the BS phase is expected to display two types of intra-trimer dipole-allowed transitions: $|w_1\rangle$-to-$|w_2\rangle$ and $|w_2\rangle$-to-$|w_3\rangle$.

We study the dynamics of the optically excited system by combining the model in Equation 1 with Ehrenfest dynamics, as discussed in reference [26, 27]. The effect of the light-pulse, which is defined by electric field $\vec{E}(r,t) = \vec{e}_A \omega \mathrm{Im}(A_o e^{-i\omega t})g(t)$, is incorporated in the model by the Peierls substitution method [29]. Here A_o is the magnitude of the vector potential, ω is the angular frequency, $\vec{e}_A$ is the direction of the electric field. The pulse shape is Gaussian fixed by $g(t) = e^{\frac{-t^2}{2c_\omega^2}}(\sqrt{\pi c_\omega^2})^{-1}$ where pulse duration defined by its FWHM= $2c_\omega\sqrt{\ln 2}$. The propagation of the single-particle wave functions $|\psi_{\sigma,\alpha,R,n}\rangle$ and the spins $\vec{S}_R$ is governed by time-dependent Schrodinger equation while the atoms are treated classically and they evolve according to Newton's equations of motion (more information in SI).

To measure the photocurrent magnitude, we calculate the evolution of the current-density $\vec{j}^{el}(t)$ which is defined at time t as $\vec{j}^{el}(t) = -\frac{e}{V}\sum\limits_{l\epsilon N_R} \vec{j}_l(t)$, where $V = d_{Mn-Mn}^3 N_R$ is the volume of the unit cell with N_R number of Mn ions and with average bond length $d_{Mn-Mn}=3.84\,\text{Å}$ between Mn ions. The current vector $\vec{j}_l(t)$ at lattice site l
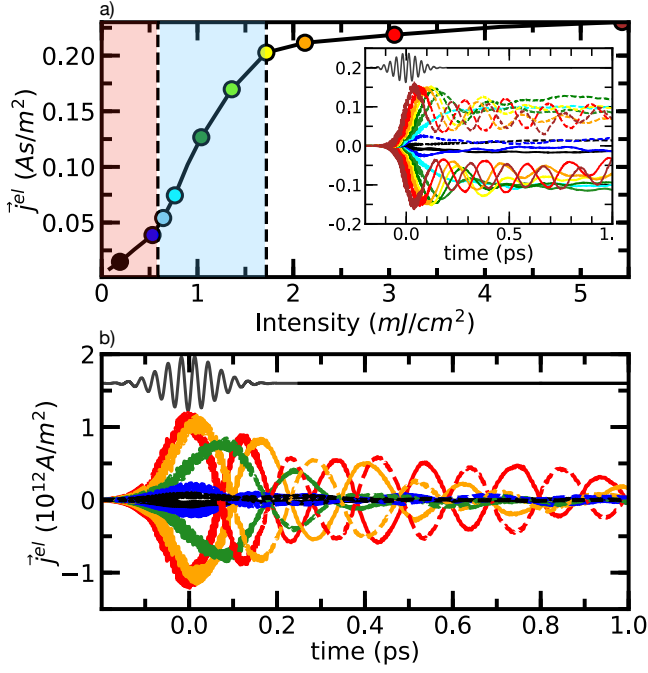
FIG. 2. Generation and evolution of photocurrent a): Integrated current-density $\int dt j^{el}(t)$ versus intensity I showing three regions, namely I (red-shaded), II (blue-shaded), and III (white-shaded) with distinct photocurrent behavior for light polarized along $\vec{a}$ direction. The time-integration is performed from the beginning till the first $\vec{j}^{el}$ maximum. Inset shows the integrated current $\int dt j^{el}(t)$ versus time t. The symbol and line colors refer to the different light intensities. b): Instantaneous current $j^{el}(t)$ versus time t. The light-pulse is shown in black in the top. The solid-and dashed-lines in the inset of left figure and in right figure show the direction $(\vec{a} + \vec{b})$ and $(\vec{a} - \vec{b})$, respectively, of the current. The colors refer to the increasing intensities with A_o=0.15 $\hbar/ea_o$ (black), 0.25 $\hbar/ea_o$ (blue), 0.35 $\hbar/ea_o$ (green), 0.50 $\hbar/ea_o$ (orange) and 0.60 $\hbar/ea_o$ (red) The corresponding light-intensities are $I = 0.19$ mJ/cm^2 (black), 0.53 mJ/cm^2 (blue), 1.04 mJ/cm^2 (green) and 2.12 mJ/cm^2 (orange) and 3.05 mJ/cm^2 (red).

is expressed as

$$\vec{j}_l(t) = \sum_n f_n(t) \sum_{l' \epsilon \langle NN \rangle} \sum_\sigma \sum_{\alpha,\beta} \frac{i}{\hbar} \Big(\psi^*_{\sigma,\alpha,l,n}(t) T_{\alpha,\beta,l,l'} \psi_{\sigma,\beta,l',n}(t)$$
$$- \psi^*_{\sigma,\beta,l',n}(t) T_{\beta,\alpha,l',l} \psi_{\sigma,\alpha,l,n}(t) \Big) d_{Mn-Mn} \vec{e}_{l-l'}. \quad (2)$$

Here, $f_n(t)$ is the instantaneous occupation of the one-particle states $|\psi_n\rangle = \sum_{\sigma,\alpha,l} |\chi_{\sigma,\alpha,l}\rangle \psi_{\sigma,\alpha,l,n}(t)$ and $\vec{e}_{l-l'} = \left(\frac{\vec{R}_l - \vec{R}_{l'}}{|\vec{R}_l - \vec{R}_{l'}|} \right)$ is the unit vector in the direction joining sites l and l'. $T_{\alpha,\beta,l,l'}$ is the hopping matrix element between e_g-orbitals α and β at sites l and l', respectively.

We simulate the photocurrent of a 12×12×4 perovskite supercell under a 100 fs Gaussian pulse and periodic boundary conditions (Γ-point k-point sampling). The photon energy was set at $\hbar\omega$=0.97 eV, where the sys-

tem shows maximum absorption. Here, we discuss results for light polarization in the $\vec{a}$ direction, with light polarization in the $\vec{b}$ direction being qualitatively similar, resulting in photocurrents that are always aligned along the bulk polarization direction. Light polarization in the $\vec{c}$ direction results in no net current because it contains a mirror plane. The current-vs-intensity behavior over a range of intensities typical of ultrafast spectroscopies separates into three distance regions (Figure 2a): region I (I=0−0.65 mJ/cm^2) where the current grows linearly with the light intensity; region II (I=0.65−1.70 mJ/cm^2) with a sharp rise in the photocurrent; region III (I=1.70− mJ/cm^2 when the photocurrent saturates.

In region I, lowest order BPVE is active; the linear dependence of current on intensity shows that processes that are second order in the electric field, namely shift and ballistic photocurrents, contribute to the photocurrent. The current direction at very low intensities is predominantly along the bulk polarization direction, $\vec{a}$. Spin dynamics are not yet active in this region, with the ground state SO remaining intact and the photoinduced dynamics is entirely driven by electrons and phonons. The electronic transitions in region I are predominantly intra-trimer $|w_1\rangle$-to-$|w_2\rangle$ and involve the charge transfer from the Mn^{3+} to Mn^{4+} I and II sites of the trimer, indicated by the solid arrow in Figure 1b.

Oscillations in the instantaneous current over a 200 fs time scale, which are driven by phonons, are already discernible in region I. These oscillations do not contribute to the net time-integrated current; to remove their contribution, we plot only the time-integrated current $\int dt j^{el}(t)$ in the current-vs-intensity plot (Figure 2a). Due to the strong el-ph coupling, the octahedral phonon modes follow the photoinduced alterations in the charge disproportion between Mn sites. Oxygen octahedra around Mn^{3+} sites, originally expanded in the ground state (Figure 1a), start to shrink upon photoexcitation, as indicated by decreased O-O bond distances $d_\parallel$ along the local trimer axes in Figure 3a. In contrast, the average O-O bond-lengths in the ab-plane around Mn^{4+} II and III sites increase as shown in Figure 3b. As soon as the octahedral deformations around Mn sites adapt to the new local charge densities, the coherent phonon modes of THz frequencies are excited. The amplitude of the excited phonon modes grows with the light intensity.

In the intensity region II (Figure 2a), the current sharply increases due to a photoinduced magnetic phase transition from the original non-collinear SO to a new collinear SO, signaling a departure from the regime of perturbative BPVE. In the new collinear SO, t_{2g} spins on Mn^{4+} III sites rotate to bridge spin-aligned trimers, originally disconnected in the ground state, forming continuous ferromagnetic zig-zag chains in the ab-plane, consisting of collinear horizontal and vertical Mn-tetramers, as shown in Figure 3d. The CO within tetramer lacks an inversion center causing asymmetric intersite electron transfer between the original trimer and the adjacent Mn^{4+} III site. As a result of this new ferromagnetic

alignment in the non-centrosymmetric ab-plane, carrier transport is enhanced, with the photocurrent being predominantly in the $\vec{a}$ direction.

The mechanism for the magnetic phase transition can be understood as follows. The photo-induced intersite electron-transfer between Mn^{4+} II and III site via $|w_1\rangle-|w_6\rangle$ and $|w_2\rangle-|w_6\rangle$ hybridization, along the trimer axes (shown by the solid black arrow in Figure 1b) triggers spin dynamics. This intersite electron-transfer is restricted to the ferromagnetic spin component. This spin-restricted electron-transfer changes the local e_g-electrons spin and perturbs the t_{2g}-spins, due to Hund's coupling, inducing the t_{2g}-spin dynamics. The evolution of the t_{2g}-spin angles between sites is shown in Figure 3c. Above a critical intensity I_o=1.35 mJ/cm^2, the perturbation on the t_{2g}-spins is strong enough to induce a magnetic phase transition within 100 fs. The spin angle fluctuations settle within 500 fs.

The electron-transfer within tetramers is sensitive to the local orbital polarization and the onsite e_g-orbital energy levels at Mn sites, which in turn depend on the phonon dynamics. As long as there is a charge-disproportion between sites within the tetramers, the phonon modes track the local charge asymmetries over time, as shown in the inset of Figure 3c, and contribute to phonon-induced photocurrent oscillations. These oscillations decay on sub-picosecond timescales, primarily due to energy loss to spin degrees of freedom.

Upon further increase in intensity (region III), the current starts saturating due to the dissipation of excited electron energy into phonon modes. As seen in Figure 3a-b, phonon-induced current oscillations grow in amplitude in region III. Further energy loss from the phonon modes into spin degrees of freedom is also evident from the sub-picosecond decay of phonon oscillations in Figure 3a-b. A secondary effect is the change in the electronic structure resulting from excited phonon modes. Upon photoexcitation in region III, the energy gap between the valence and conduction bands is reduced. This detunes the resonance between the light field and the peak absorption energy, which reduces the absorption coefficient and photocurrent at high intensities.

Overall, the magnetic phase transition results in an enhancement of photocurrent compared to other materials that display BPVE in the perturbative limit. The photoresponsivity $R_p = \frac{1}{I}\int \vec{j}^{el}(t)dt$, where the time-integration is performed over light-pulse duration, calculated for intensity I=2.12 mJ/cm^2 at the time of current saturation in region III is 10 mA/W, an order of magnitude higher the photoresponsivity for the known ferroelectric oxide BiFeO$_3$ [5].

To measure the contribution of the phonon and spin-assisted processes, we repeat the simulations keeping either atoms or spins or both fixed (Figure 4). With constrained spins, there is clearly no photoinduced magnetic phase transition. Moreover, with fixed atoms, we do not find any magnetic phase transitions either, for the light intensity range covered in the present work, sug-
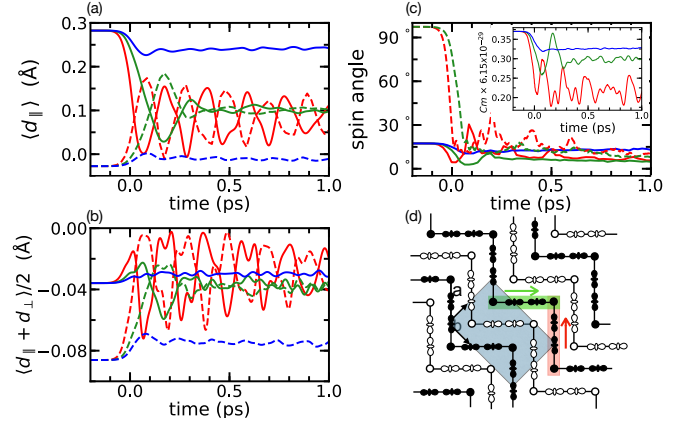

FIG. 3. Dissipation of the excited-electrons energy into the octahedral phonon modes and t_{2g}-spins. a): O-O bond expansions $d_\parallel$ (see Figure 1c) along the local trimer axes around Mn^{3+} (solid-lines), Mn^{4+} I (dashed-lines). b): average O-O bond expansion $d_{\parallel_{ab}} = \langle\frac{d_\parallel+d_\perp}{2}\rangle$, around Mn^{4+} II (solid-lines) and Mn^{4+} III sites (dashed-lines). c): Evolution of the average intra-trimer spin angles (solid-lines) and inter-trimer spin angle along the direction of trimer (thick-lines). The inset shows evolution of average local dipole moment $P_l = \langle\sum_i^5 \rho_i \vec{r}_i\rangle$ of tetramer units, indicated in red and green in panel d. The colored lines refer to the increasing intensities with 0.53 mJ/cm^2 (blue), 1.04 mJ/cm^2 (green) and 3.05 mJ/cm^2 (red). d): Photo-induced collinear SO in the ab-plane. Spin-up (spin-down) sites are indicated by white (black). The ab planes are antiferromagnetically coupled in $\vec{c}$ direction.
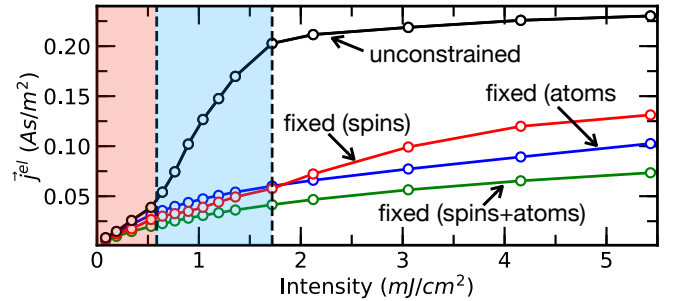

FIG. 4. Integrated current-density $j^{el}(t)$-vs-intensity during the light-pulse for the different cases. The unconstrained case shows three intensity regions, I (red-shaded), II (red-shaded), and III (white-shaded) with distinct current behavior.

gesting that phonon dynamics is crucial for the phase transition. This is because the photoinduced octahedral deformations bring $|w_1\rangle$, $|w_2\rangle$ and $|w_6\rangle$ states, involved in the $|w_1\rangle-|w_6\rangle$ and $|w_2\rangle-|w_6\rangle$ hybridization, energetically closer, strengthening the intersite coupling between Mn^{4+} II and III sites (see solid arrow in top-right Figure 1), thus facilitating the magnetic phase transition. The photocurrent in the cases with constrained atoms

or spins is linear with intensity, with no current saturation, implying that they remain in the perturbative BPVE limit over the range of simulated intensities.

In the absence of the spin and lattice dynamics, as in the fixed (atoms+spins) case in Figure 4, the photocurrent is purely the shift current along with other higher-order contributions. The additional current in the fixed (spins) and fixed (atoms) cases reflects the individual contribution from the phonon-assisted and spin-assisted processes, respectively. We see that both phonons and spins act to increase the overall photocurrent significantly, even in this perturbative limit, with the spin-assisted processes doubling the current of the fully constrained case. At low light intensities (region I), the spin contribution to the current exceeds the phonon contribution. However, for higher intensities, the phonon-assisted ballistic current becomes larger compared to its spin counterpart. In the absence of phonon dynamics, as for the fixed (atom) case, the excited electrons dissipate energy directly into the spins generating the spin-assisted ballistic current, see Figure 4. In all of these cases, the direction of current during the light pulse remains predominantly along the bulk polarization direction.

Our results highlight the significance of the photoinduced effects driven by spin and lattice dynamics in BPVE, suggesting the potential for controlling photovoltaic materials responses with tunable excitations and interactions. A design strategy for large BPVE suggested by these results is to look for systems with strong correlations that can undergo optically induced phase transitions at low intensities producing an abrupt change in the photocurrent like in the case studied here. Compared to other nonpolar modes, the electronic properties in complex oxides are strongly linked to the JT distortions. Our study reveals that the coherent dynamics of the excited JT and breathing modes contribute to the phonon-assisted ballistic photocurrent currents. Transition metal oxides such as manganites or nicklates, with spin orders in ground and excited states, are candidates to show spin-assisted BPVE as demonstrated here.

In conclusion, we have shown how a combination of spin- and phonon-induced processes can substantially enhance the bulk photovoltaic effect, using a non-perturbative methodology. The real-time simulations of a strongly correlated system show that photoinduced phase transitions, which are generally ignored in perturbative theoretical methods, significantly impact the photocurrent generation and its evolution. Understanding the effect of the transient spin and lattice dynamics on the dynamical nature of the band structure can be exploited for desirable photovoltaic properties by tuning the correlations and interactions in correlated systems through targeted materials design.

[1] A. M. Burger, R. Agarwal, A. Aprelev, E. Schruba, A. Gutierrez-Perez, V. M. Fridkin, and J. E. Spanier, Science Advances **5**, eaau5588 (2019).

[2] R. von Baltz and W. Kraut, Phys. Rev. B **23**, 5590 (1981).

[3] J. E. Sipe and A. I. Shkrebtii, Phys. Rev. B **61**, 5337 (2000).

[4] S. M. Young and A. M. Rappe, Phys. Rev. Lett. **109**, 116601 (2012).

[5] S. M. Young, F. Zheng, and A. M. Rappe, Phys. Rev. Lett. **109**, 236601 (2012).

[6] L. Z. Tan, F. Zheng, S. M. Young, F. Wang, S. Liu, and A. M. Rappe, npj Computational Materials **2**, 16026 (2016).

[7] V. I. Belinicher and B. I. Sturman, Soviet Physics Uspekhi **23**, 199 (1980).

[8] B. I. Sturman, Physics-Uspekhi **63**, 407 (2020).

[9] Z. Dai, A. M. Schankler, L. Gao, L. Z. Tan, and A. M. Rappe, Physical Review Letters **126**, 177403 (2021), publisher: American Physical Society.

[10] A. M. Cook, B. M. Fregoso, F. de Juan, S. Coh, and J. E. Moore, Nature Communications **8**, 14176 (2017).

[11] S.-J. Gong, F. Zheng, and A. M. Rappe, Phys. Rev. Lett. **121**, 017402 (2018).

[12] T. Barik and J. D. Sau, Physical Review B **101**, 045201 (2020), publisher: American Physical Society.

[13] R. A. Kaindl, M. A. Carnahan, D. Hägele, R. Lövenich, and D. S. Chemla, Nature **423**, 734 (2003).

[14] S. Leinß, T. Kampfrath, K. v.Volkmann, M. Wolf, J. T. Steiner, M. Kira, S. W. Koch, A. Leitenstorfer, and R. Huber, Phys. Rev. Lett. **101**, 246401 (2008).

[15] P. Buczek, A. Ernst, P. Bruno, and L. M. Sandratskii, Phys. Rev. Lett. **102**, 247206 (2009).

[16] G. Fischer, M. Däne, A. Ernst, P. Bruno, M. Lüders, Z. Szotek, W. Temmerman, and W. Hergert, Phys. Rev. B **80**, 014408 (2009).

[17] C. Verdi, F. Caruso, and F. Giustino, Nature Communications **8**, 15769 (2017).

[18] T. Kampfrath, A. Sell, G. Klatt, A. Pashkin, S. Mährlein, T. Dekorsy, M. Wolf, M. Fiebig, A. Leitenstorfer, and R. Huber, Nature Photonics **5**, 31 (2011).

[19] M. Reticcioli, U. Diebold, G. Kresse, and C. Franchini, arXiv e-prints , arXiv:1902.04183 (2019), arXiv:1902.04183 [cond-mat.mtrl-sci].

[20] D. Daranciang, M. J. Highland, H. Wen, S. M. Young, N. C. Brandt, H. Y. Hwang, M. Vattilana, M. Nicoul, F. Quirin, J. Goodfellow, T. Qi, I. Grinberg, D. M. Fritz, M. Cammarata, D. Zhu, H. T. Lemke, D. A. Walko, E. M. Dufresne, Y. Li, J. Larsson, D. A. Reis, K. Sokolowski-Tinten, K. A. Nelson, A. M. Rappe, P. H. Fuoss, G. B.

Stephenson, and A. M. Lindenberg, Physical Review Letters **108**, 087601 (2012).

[21] S. Priyadarshi, K. Pierz, and M. Bieler, Physical Review Letters **109**, 216601 (2012).

[22] S. Mori, C. H. Chen, and S.-W. Cheong, Nature **392**, 473 (1998).

[23] P. G. Radaelli, G. Iannone, M. Marezio, H. Y. Hwang, S.-W. Cheong, J. D. Jorgensen, and D. N. Argyriou, Phys. Rev. B **56**, 8265 (1997).

[24] M. T. Fernández-Díaz, J. L. Martínez, J. M. Alonso, and E. Herrero, Phys. Rev. B **59**, 1277 (1999).

[25] M. Sotoudeh, S. Rajpurohit, P. Blöchl, D. Mierwaldt,

J. Norpoth, V. Roddatis, S. Mildner, B. Kressdorf, B. Ifland, and C. Jooss, Phys. Rev. B **95**, 235150 (2017).

[26] S. Rajpurohit, C. Jooss, and P. E. Blöchl, Phys. Rev. B **102**, 014302 (2020).

[27] S. Rajpurohit, L. Z. Tan, C. Jooss, and P. E. Blöchl, Phys. Rev. B **102**, 174430 (2020).

[28] T. Hotta and E. Dagotto, arXiv e-prints , cond-mat/0212466 (2002), arXiv:cond-mat/0212466 [cond-mat.str-el].

[29] R. Peierls, Zeitschrift für Physik **80**, 763 (1933).